A design study of a 1-m² Multi-Wire-Proportional-Chamber Position-Sensitive-Neutron-Detector (MWPC-PSND)

Gregor Nowak[1*], *Irina* Stefanescu[2], *Andreas* Beldowski[1], *Jochen* Fenske[1], *Richard* Hall-Wilton[3] and *Martin* Müller[1]

[1]Helmholtz-Zentrum Hereon, WPE & TKA, 21502 Geesthacht, Germany
[2]European Spallation Source ERIC (ESS), Detector Group, 22100 Lund, Sweden
[3]Fondazione Bruno Kessler, Sensors & Devices Centre, 38123 Trento, Italy

Abstract. Neutron detection by MWPC based on $^{10}B_4C$ coatings can surpass in performance the one utilising ^{3}He-gas in terms of position resolution and count rate capability at similar detection efficiency [1-3]. The use of m²-size foils coated by $^{10}B_4C$ demands the development of a mechanical concept to avoid deformations of the neutron sensitive surface due to their own weight and the electrostatic forces resulting from high voltage for operation. To preserve a flat shape of the converter, a pressure gradient is applied between its both sides [4]. The design shall allow a stacking of detection modules consisting of sequenced elements [converter/x-y-multi-wire planes/converter] in few mm proximity. A multiple stacking of the detector modules is needed to accumulate a sufficient high detection efficiency for diffraction with thermal neutrons over the entire detector [2]. The MWPC is planned to have fifteen detection modules corresponding to an efficiency equivalent of 30 converters coated with 1.2 µm of $^{10}B_4C$. Efficiency simulations of a converter coating thickness-profile from 0.6 µm up to 1.2 µm prognoses a conversion rate up to 50 % for thermal neutrons and the presented design parameters of the 1-m² MWPC allow a position resolution of 2 mm.

1 Introduction

Multi-Wire-Proportional-Chambers (MWPC) are used for a two-dimensional position-sensitive detection of radiation fields [5]. They consists of corresponding x- and y-sensitive detection wire planes immersed in stopping-gas, which releases charged particles when hit by ionizing radiation. The released primary electrons from ionised gas are accelerated towards the closest detection wire of a wire plane, which is set under high voltage (HV). The radial gradient of the electric field surrounding a detection wire is the main source of kinetic energy gain for the primary ionisation electrons. The acceleration and charge multiplication process is confined to a distance of a couple of hundreds µm around the detection wire [6]. The charge multiplication starts when the kinetic energy transferred by the electric field gradient to the primary ionisation electrons is high enough to further ionise the gas atoms and give rise to a charge avalanche. The process of generating electrons close to the detection wire in a sufficient number to trigger electric pulses in modern amplification electronics is called gas amplification. In the following sections, the neutron-sensitivity and neutron-event position-encoding techniques of a MWPC will be discussed. This introduces the special type of a MWPC, which offers a 2D-position sensitive neutron detection.

1.1 Techniques for neutron-sensitivity of MWPC

Neutron-sensitive MWPCs for a 2D-position registration are very useful for application in various neutron scattering techniques as conducted in neutron scattering research centers like ILL (France) [7], SNS (USA) [8], MLZ (Germany) [9] or J-PARC (Japan) [10] and in many more places worldwide and soon at the European Spallation Source (ESS) in Lund (Sweden) [11]. Their advantage over other neutron detector technologies are the low gamma sensitivity and a fast response compared to scintillator detectors as well as a spatially more homogenous response with a higher spatial resolution compared to tube detectors on the costs of sophisticated manufacturing techniques. The sensitivity of a MWPC to (thermal) neutrons is achieved by the introduction of an additional material in the gas volume, which converts the uncharged neutrons into charged primary particles by an appropriate conversion reaction [12]. The neutron sensitivity of a MWPC goes on top on the sensitivity for ionizing radiation. The design of a MWPC-Position Sensitive Neutron Detector (PSND) therefore has to trade-off strongly the sensitivity for neutrons over the sensitivity for other ionizing radiation fields as emitted by many parasitic sources including high-energy cosmic particles [13] in the field of use. Typical isotopes for this application are the ones with a large cross-section for neutron induced

* Corresponding author: Gregor.Nowak@hereon.de

fission, possessing simultaneously a low-Z number and being in a low density aggregate state, thus offering a low absorption probability for gamma radiation [6]. Therefore, they are the choice for neutron converting materials [14]. Reactions of the type $^{x}Y(n,\alpha)^{(x-3)}$ are in the focus for neutron conversion processes. Conventionally, the ^{3}He-gas or a ^{10}B-containing material are used for the conversion of neutrons into charged particles [15-16]. In addition, fissionable materials like $^{233\text{-}238}$U, ^{157}Gd, or ^{6}Li-isotope, etc. are in use [17].

Neutron detectors based on ^{3}He- or $^{10}BF_3$-gas have been extensively used for detection of thermal neutrons. However, further deployment of such detectors is currently constrained by the dramatic increase of ^{3}He-price (so called "^{3}He-crisis" [18]). Moreover, in case of $^{10}BF_3$-gas, the toxicity of larger gas volumes at places of use gets an issue with improved modern safety standards [19]. One way to construct large area PSND under these circumstances is to switch from gas to solid-state converter containing ^{10}B. A drawback of the switch to solid-state converter is the accompanied strongly limited (to micrometres) ion-escape-length (=ion travel range) from the conversion point in the coating prior the primary ions enter the stopping-gas-volume for the detection process. The short ion escape length in the converter material limits the probability for the ions created far away from the converter/stopping-gas-interface to enter the adjacent detection gas volume to trigger the detection process. The maximum efficiency of this detection process with ion generation in solid converter and their transfer to stopping gas scales with the ion population reaching out the stopping gas volume. Nevertheless, ion-range simulations and the good controllable deposition properties of $^{10}B_4C$ coatings on the lightweight material aluminium [1, 20-22] shifted the development of PSND in the last decade towards $^{10}B_4C$-coating-based detection techniques [22-24]. The good sputtering properties supports the manufacturing of large area converters. In ^{10}B-based neutron converters, the following Neutron- induced fission-reaction takes place [25] (with kinetic energy in the round brackets):

$$n + {}^{10}B \rightarrow \begin{cases} {}^{7}Li\,(840\ keV) + \alpha(1470\ keV) + \gamma(480\ keV), & 94\ \%\ (A) \\ {}^{7}Li\,(1015\ keV) + \alpha(1770\ keV), & 6\%\ \ (B) \end{cases} \quad (1)$$

The charged-particles emerging from the (n,^{10}B)-reaction ionize the stopping-gas thereby generating the primary electrons, which set off the charge avalanche near the wires and makes possible the detection process [5].

1.2 Size of active area and position resolution

The size of the active area of a PSND at a constant sample-detector distance defines the accessible range of wave-vector transfers covered in one detector configuration for a given scattering/diffraction experiment at a chosen pulse and wavelength band [26]. Therefore, the application of large area (m^2-size) detectors at Time-of-Flight (ToF)-diffractometers contributes substantially to a shortening of the acquisition time in a measurement [27]. The current state-of-the-art engineering neutron-diffraction beam lines like BEER [28], TAKUMI [29], IMAT [30], SMARTS [31], ENGINE-X [32] or VULCAN [33] offer a 1-2 m sample to detector distance to accommodate the typical size, complex engineering in-situ sample environment. These instruments offer a resolution $\Delta Q/Q$ down to 0.1% for thermal neutrons. The approximation for the resolution of the wave-vector transfer for a ToF-diffractometer is expressed by Eq.(2) (see [26], page 142 or [34], page 107). This relation can be used to estimate the upper limit for the spatial resolution of the detector for a set of source and diffractometer parameters (operational wavelength band, pulse length) in order to achieve the required $\Delta Q/Q$:

$$\left(\frac{\Delta Q}{Q}\right)^2 = \left(\frac{\Delta L}{L}\right)^2 + \left(\frac{\Delta t}{ToF}\right)^2 + (\Delta\Theta\cot(\Theta))^2 \quad (2)$$

with Δt = chopper pulse length, ToF = Time of Flight from chopper to detector, L= Length of flight path, ΔL = uncertainty in flight path from the chopper to the detector, $\Delta\Theta$ = recorded Bragg-peak width at the detector position, folded with detector resolution, incident beam divergence and scattered beam size and Θ = Bragg angle of the reflection. For long instruments (>100 m), the first term of Eq.(2) contributes with about 0.01 % to $\Delta Q/Q$. The main variable contributions to $\Delta Q/Q$ in Eq.(2) result from the variations of the pulse length Δt and to the same order of magnitude from the Bragg-peak width $\Delta\Theta$ in the scattering plane, which is typically dominated by the fixed horizontal beam divergence of about 5 - 25 mrad. At a distance of 2 m between sample and the detector, a position resolution of a couple of mm in the horizontal scattering plane contributes only with a few mrad to the Bragg-peak width $\Delta\Theta$, but it allows for a sufficient spatial sampling of the Bragg-peak shape in the scattering plane. This motivates the envisaged couple of mm large position resolution of a modern ToF-diffraction detector.

1.3 Techniques for 2D-position encoding of MWPC-PSND

For the two-dimensional neutron-event position determination in a MWPC-PSND, two methods of position encoding are conventionally used.

The most common position encoding technique is the resistive-wire method. There, the accumulated charge is deposited on the detection wire closest to the location of the neutron capture by the converter material. The deposited electron charge is measured after its travel to both ends of the wire as a voltage pulse-height [35]. The voltage pulse-heigths measured at each end of the detection wire are proportional to the ratios of the electric charges that pass through the corresponding fraction of the total length measured from the detection point and their specific Ohmic-resistance. The relative position of the neutron event along the wire is given by the ratio of the partial and the total (sum) pulse-heights.

This method requires that the number of readout channels and Analog-to-Digital Converters (ADCs) equals the number of wire-ends in the detector (e.g., twice the number of single wires).
A second type of position encoding in a MWPC-PSND is the delay-line method [6]. In this method, one end of every single detection wire is connected to a unit cell of a delay-line ladder circuit consisting of a resistive, capacitive and inductive element. The number of the unit cells in the delay-line ladder circuits corresponds to the number of wires in each of the both x- and y-wire planes. At both ends of this ladder circuit (= delay line) a pre-amplifier is connected. Its function is to increase the microvolt pulse passed and damped through a certain number of unit-cells to a millivolt level as needed for the further signal processing. The resistive, capacitive and inductive elements within the delay-line unit cell are chosen so that the propagation speed of a typically shaped event pulse is slowed down to about 1 ns per unit cell transient. Therefore, the traveling time of an event-pulse towards the ends of the delay-line fed-in by a detection wire at a certain position of the delay-line circuit increases by the integer number m of transient times (here: 1 ns) resulting from the passage through m delay-units [6]. The precise measurement of the time difference between the delayed pulses at the ends of the delay-line allows determining the number m of passed delaying unit cells of the delay-line circuit and therefore determining the number m of passed wires with their specific geometric distance from each other. For a single detection module, the x- and y-position components of a certain neutron event can be determined within the same time-correlation radius corresponding to the time-delay of a whole x- or y-delay-line length. The registered arrival-time differences for the x- and y-components become converted by the number of passed delay-time steps (m_x and m_y) and by the corresponding geometric wire-pitch in a wire-plane (here: 2 mm) to (x,y)-event positions in mm within one detection module. The position determination of a neutron event using x- and y-delay-lines for one detection plane is reduced practically to a time difference measurement with a Time-to-Digital-Converter (TDC) unit instead of pulse-height determination using many ADCs, as in the case of the resistive wire scheme.
The advantage of the delay-line position-encoding over resistive-wire scheme becomes evident for detector systems consisting of a large amount of detection wires. In these systems, the delay-line techniques requires a much smaller number of amplifiers compared to resistive-wire method since one delay-line serves as pulse collector for many hundreds of detection wires and needs only one amplifier at every one of its two ends. In contrast to this, the resistive-wire method needs one amplifier at each end of every one of the many hundreds of detection wires. This leads to a much lower number of read-out channels and connecting feedthroughs between the detection volume and the outside space of the detector for the delay-line method compared to the resistive-wire method. With modern electronics and Printed Circuit Board (PCB) layout techniques, delay-lines circuits with their resistive, capacitive and inductive character can be realized on PCB without using individual resistors, capacitors and inductances. A corresponding, geometric guidance of the conductor paths on the PCB-board with terminals for the detection wires replaces all three electric elements.

1.4 Count-rate capability of a MWPC

The count-rate capability of a single detection module is derived from the detection performance of the TDC for a single pulse in the x- and y-delay-line read-out. For typical conversion process times (from neutron hit to electron avalanche end on the detection wire) of the order of 80 - 100 ns and a total length of the delay-line of e.g., 500 ns, the count-rate capability of a single-detection module can be estimated to 150 – 200 kcps [36-38]. Therefore, the full detector assembly, which should consist of fifteen independent detection modules giving rise to a global count rate capability of 15 times 150 – 200 kcps can be estimated to max. 3 Mcps.
The constructional advantage of delay-line read-out holds as long as the event-rate on a single detection-wire-plane stays below the above estimated value. For higher count-rate situations, the single-resistive-wire read-out coupled to fast but costly ADC is preferable.

2 Development of the detector design

The conception and description of the detector design discussed in this study follows the basic, methodical engineering order as applied for the design development of complex machines: from interior to the exterior [39-40]. Therefore, the simulations of the ion traces from the converter to the detection wires are the starting point in chapter 2.1 for the interior detector design. These simulations define the converter thickness and the converter-to-wire distance. In chapter 2.2, the next higher hierarchic level of the detector assembly is considered; here the detection performance is simulated resulting from the geometric design of the detection module and the internal organisation of detection modules within the detector. Finally, the mechanical design of the detection modules and for the detector housing (the exterior) is discussed in chapter 2.3. The mechanical design of the exterior shall ensure a stable operation of the detector in its environment.

2.1 Simulations of the ion travel ranges involved in the detection process

The ion-stopping process in solids and gases is governed by the strong and repulsive Coulomb-interaction between the positive ions and the positive nucleus of the stopping medium. This give rise to a stopping-power curve with a Bragg-like shape including a sharp cut-off energy. This leads to a strong correlation between the ion-energy and the ion-travel range in the stopping medium [41]. To ensure an efficient and localized electron collection by the detection wire system, the ranges and shapes of the traces of the released ions in and out of the conversion coating need to be evaluated. The ion ranges in the stopping gas are important to fix an appropriate detection-wire to converter distance. The

divergence of the ion tracks allow us to estimate the lower limit of the position resolution given by the gas amplification. The kinetic energies of the ions escaping from the point of conversion in the converter, which is given by the conservation of momentum and energy for the nuclear reaction Eq.(1) and the stopping power in solid $^{10}B_4C$ are reported in [42-43]. For the branches (A) and (B) of the conversion reactions in Eq.(1), the maximum ranges of α and ^{7}Li ions in solid ^{10}B coating are [43]:

Branch (A) of Eq.(1):

- Ion range for α-particle: 3.2 µm and ^{7}Li-ion: 1.5 µm

Branch (B) of Eq.(1):

- Ion range for α-particle: 3.9 µm and ^{7}Li-ion: 1.7 µm

In order to allow the ions produced in both reaction branches described above to escape from the conversion layer with enough kinetic energy and ionise the adjacent detection gas, the converter thickness is chosen below the shortest ion-range in the coating. As demonstrated in [1,6,14,44], the appropriate $^{10}B_4C$ converter thickness for thermal neutron detectors with a gas-amplification processes at 1 bar pressure in adjacent to the stopping gas volume is 1.2 µm $^{10}B_4C$. This $^{10}B_4C$ converter coating thickness is a reasonable trade-off between neutron capture probability in the converter and a high enough ion escape efficiency out of the converter combined with a high enough kinetic energy of the ions emitted from a single $^{10}B_4C$ layer.

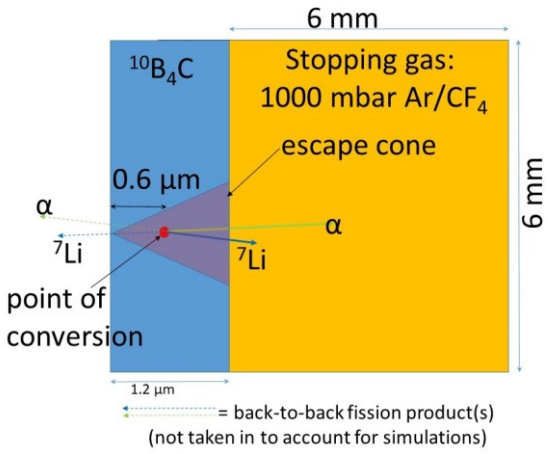

Fig. 1. Simulation set-up with point of conversion, 1.2 µm thick $^{10}B_4C$ coating, 6 mm x 6 mm stopping gas volume and the anticipated escape cone of the ions.

The simulations of ion-tracks consider the $^{10}B(n,\alpha)^7Li$-conversion in Eq.(1) to take place at 0.6 µm depth from the surface of a 1.2 µm thick $^{10}B_4C$ layer. The ions enter from left orthogonally (Fig. 1) in to a 6 mm x 6 mm extended stopping-gas volume. This configuration should cover the most in all likelihood conversion situation with the ion-travel range in the stopping-gas. Indeed the conversion can take place at any depth of the 1.2 µm thick $^{10}B_4C$, but statistically the probability for the conversion reaction increases with higher penetration depth of the neutron. At the same time for the neutron detection process also the ion-escape-process and its descending probability with the larger depth of the conversion point from the surface has to be taken in to account. The ion ranges from branch (A) and (B) represent the upper limit for travel paths of the corresponding ions in the solid converter. Because of this, these maximum travel ranges and the converter thickness span in the directional space an escape cone (with maximum probability for the ion transfer in to the stopping gas) oriented with its axis parallel to the converter normal direction, with an opening angle resulting from 2 times the cosine between the converter thickness (here: 1.2 µm) and the maximum travel range (here for the α-particle from branch (B): 3.9 µm). That is an angle of 72° from the normal direction of the converter plane or a cone described by a solid angle of 144° as shown in Fig. 1.

Typically, the ions from the solid converter within this solid angle/cone will enter the stopping-gas volume. But only those with the shortest travel range in the solid (elongation of the orthogonal direction to the converter plane) have the highest kinetic energy left for the travel in the stopping gas and generate consequently the longest ion tracks there. These ions are taken into account in the TRIM-simulations.

Due to the large surface of the envisaged detector housing and the m^2-size neutron entrance window, the limitations by breaking stress of constructional materials need to be considered. The structural materials taken into account allows for a maximal possible pressure gradient between the inside space of the detector housing and a variable ambient pressure environment to about Δ ±100 mbar. In summary, the simulations of ion ranges in the detector volume filled with the stopping-gas are performed under ambient pressure condition, at 1000 mbar Ar/CF_4 (80%/20%) using the TRIM-software [45-46] an under the assumptions that:

- the conversion process takes place 0.6 µm from the surface of the solid, 1.2 µm thick $^{10}B_4C$-converter
- the ions travel after generation through the solid conversion coating and enter orthogonally oriented into the 6 mm x 6 mm extended stopping gas volume
- the ions travel and get stopped in the stopping gas volume adjacent to the $^{10}B_4C$ surface consists of Ar/CF_4 (80%/20%) at 1000 mbar

The corresponding ion tracks and their ranges in the stopping gas volume, called "Target depth" for a volume box of 6 mm x 6 mm are presented in Fig.2 and Fig.3. The visualization of the ion tracks in Fig.2 demonstrates clearly that the high kinetic energy of the α-particles gives rise to a less divergent ion beam in the stopping process compared to the ^{7}Li-ions normalized to an identic ion range. A strong straggling effect of the ion trajectories appears in the last tenths of the travel range. In Fig.3 is demonstrated, that the straggling parameter decreases with both, the decrease of the ion weight and

increase of kinetic ion energy. Fig.2 and 3 represent the primary charges only.

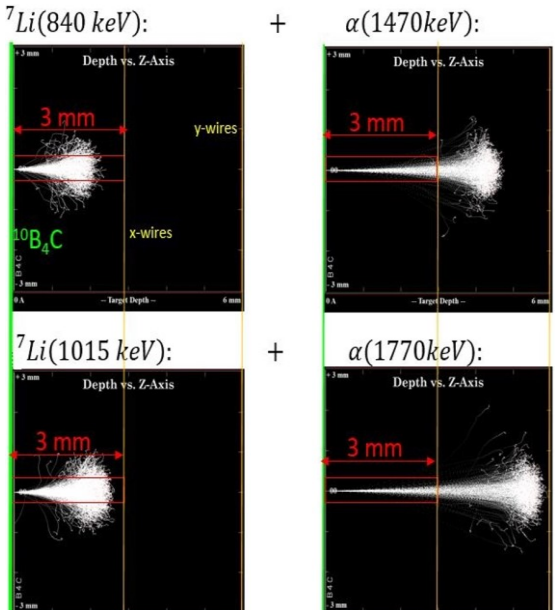

Fig. 2. Simulated tracks for α and ^{7}Li-ions by TRIM-software for (A) and (B) branch of the ^{10}B(n,α)^{7}Li-reaction in Eq.(1) taken place at 0.6 µm depth from the surface of a 1.2 µm thick $^{10}B_4C$ layer. The ions enter from left orthogonally in to a 6 mm x 6 mm extended Ar/CF_4 (80%/20%) at 1000 mbar gas volume (black background). The green bar on the right hand side in all plots marks the $^{10}B_4C$ coating and the yellow bar marks the x-detection wires at 3 mm and y-detection wires at 6 mm away from the ion emitting $^{10}B_4C$ coating. Top row for branch (A) and bottom row for (B) of reaction Eq.(1).

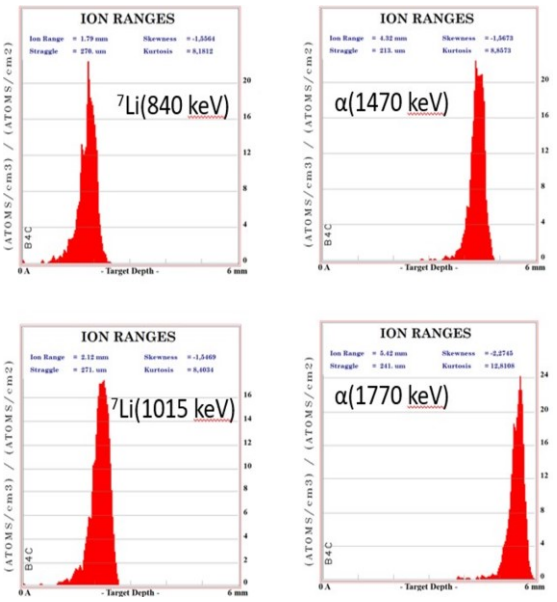

Fig. 3. Ion ranges histograms simulated by SRIM software for (A) and (B) branch of the ^{10}B(n,α)^{7}Li-reaction in Eq.(1) taken place at 0.6 µm depth from the surface of a 1.2 µm thick $^{10}B_4C$ layer. The ions enter from left orthogonally in to a 6 mm extended Ar/CF_4 (80%/20%) at 1000 mbar gas volume. The x-axis of each of these histograms represent the normal distance from the $^{10}B_4C$ converter surface (x = 0 mm) in the stopping gas volume within the range of 0 – 6 mm. Top row for branch (A) and bottom row for (B) of reaction Eq.(1).

The gas ionisation and amplification processes are not included in the TRIM-calculations in Fig. 2 and 3. However, the primary ion tracks can be regarded as origins of the gas amplification and charge avalanches if they are located close enough to the detection wire. Therefore, the radial distribution of these charges close to the detection wires influences the number of wires collecting the signal resulting from the detection process. This is quantified by the radial straggle parameter (in µm) [47] mentioned in Fig.3. Therefore, the simulated radial straggling parameter within the range of 210 – 270 µm can be regarded as the lowest value for a position resolution limit resulting from the gas ionization process when projected on a detection wire-plane. At the end of the ion-tracks, the charge cloud is enlarged to a diameter of about 1.8 mm which is less than the detection wire pitch. The range of the straggling parameter and the shape of the ion tracks ensures that the envisaged 2 mm position resolution of the detector, which corresponds to the wire-pitch in a x- or y-wire plane, is not impaired by the gas ionization process. For the stopping gas considered in these calculations, Ar/CF_4 (80%/20%) at 1000 mbar pressure, the ions are confined in a range of 1.8 - 5.5 mm distance in forward direction from the $^{10}B_4C$ converter surface.

It is worth mentioning that the position resolution that could be achieved with MWPC with $^{10}B_4C$-coated cathodes was intensively studied in the GEANT4 simulations of a detector designed for neutron diffraction studies [48]. In that study, the detector unit consisted of two thin identical wire counters sharing a segmented cathode and enclosed in a common housing filled with Ar/CO_2 (80%/20%) gas. The wire planes were positioned at a distance of 3.5 mm from the Boron converter and the distance between the wires was 17 mm. The full detector had cylindrical geometry and consisted of several detector units placed vertically around the sample and titled such that the angle between the Boron converter and the incoming neutron beam was 10°, as shown in Fig. 3 of [48]. Due to the tilting of the segment, the projection of the coated side on the entrance window of the detector becomes proportional to the product between the wire pitch and tan(10°). This gives rise to a horizontal spatial resolution of ~2.1 mm (FWHM). GEANT4 predicted a value of 2.96(6) mm (FWHM) for the spatial resolution of the proposed design, which was investigated by scanning across the wires with a collimated beam and recording the events collected by each wire, see Fig. 7 in Section 3.2 of [48]. That result is a good indication that spatial resolutions below 3 mm can be achieved with MWPC with ^{10}B-coated cathodes. We believe that this value can be further refined by replacing the CO_2 quenching gas with one with a higher stopping power, such as CF_4.

For an optimal trade-off between position resolution and charge accumulation on the detection wire, distances of 3 mm and 6 mm for the x- and y-wire-planes with respect to the converter surface seem to be the best compromise. The relative geometric configuration (stacking sequence) of the x- and y-detection wire-plane confined between the two, face-to-face oriented converters, within one detection module is as following:

[*n*-converter/3mm-gap/
/x-wire-plane/**3mm-gap**/y-wire-plane/
/3mm-gap/(*n*+1)-converter]
(3)

where *n* and (*n*+1) numerate the converter with in the full detector assembly in the detection module *n* (with *n* = 1 for the first module hit by neutrons). The stacking sequence is mirror-symmetric with respect to the central **3mm-gap** in Eq.(3), which is found between the x- and y-wire planes. This mirror symmetric configuration with respect to the central **3mm-gap** allows for an equal charge distribution on both x- and y-detection wire planes from both face-to-face oriented $^{10}B_4C$ coatings.

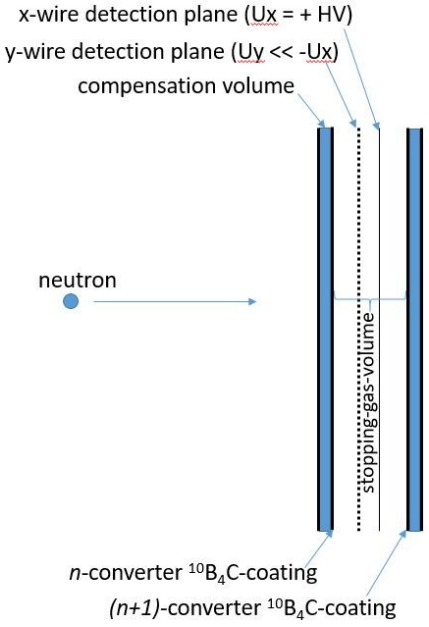

Fig. 4. Cross-section cut through one detection plane with stopping-gas-volume and two adjacent compensation volumes (blue shaded space) with $^{10}B_4C$-converter coatings and high voltage supply for x- and y-wires planes. The sequencing and spacing is as described in formula (3) above.

The stacking sequence Eq.(3) is a building block of a modular-designed detector, which consist of *n* of such detection modules. These detection modules are immersed in a common stopping-gas volume. The resulting converter-face-to-face-distance of 9 mm (see Eq.(3)) defines the ToF-timing precision within one detection module and therefore for the entire detector assembly, since the origin of an conversion event is untraceable for the detection wire system to the particular *n* or (*n*+1) converter. The back-to-back distance of adjacent detection modules is 10 mm (not included in the stacking sequence Eq.(3) above). This 10 mm-space contains the compensation volumes, which will be introduced in the next section.

The gas-gaps between the wire-planes and the converter-surfaces have to be kept constant during the detector operation. As already mentioned above, during the operation of the detector, one of the two wire-planes of a detection module is set under HV in order to accelerate the primary electrons and increase their kinetic energy to a value, which is high enough to set-off secondary gas ionisation and amplification. The electric field between the converter plane, held at ground potential, and the wire-plane under high-voltage, gives rise to an attractive force between these two components. During the detector operation this can lead to a non-uniform converter-to-wire distance (gas-gap), which results in an inhomogeneous detection efficiency distribution over the entire detection plane. To counteract the approach of the detection wires to the converter surface, a patented compensation volume design, had been developed by the Hereon research centre [4]. The compensation volume is allocated, as presented in Fig. 4, behind each converter plane and it is completely separated from the detection gas volume. The gas pressure in these compensation volumes can be adjusted individually and independently from the gas pressure in the detection volume in front of the converter. The application of a lower pressure in the compensation volume compared to the detection volume pulls the converter plate away from the detection wire planes and counteracts the attractive force resulting from the electric field between these two detection module components. The size and direction of the pressure gradient between the detection and compensation volumes separated by the converter plate can be set according to a feedback signal resulting from the converter deflection measured by means of laser spot shifts on the backside of the converter plate. This deflection control system for the converter plate is installed in every one of the fifteen detection modules. It allows the individual adjustment of every module. For a detailed description of the construction and operation of this system, the reader is asked to consult the reference [4].

2.2 Efficiency simulations of the detection modules using GEANT4

The ions-track simulations in the previous section for the $^{10}B_4C$-coating and the Ar/CF_4 (80%/20%) stopping-gas were performed with the help of the TRIM/SRIM software package to determine the distance between the converter surface and the detection wire-planes that is necessary in order to achieve the desired electron yield from the detection event on the detection wires.

In this chapter, the simulations on the next higher hierarchic level (at the level of the whole detector) are described. They were conducted in order to assess the neutron-detection performance of the complete detector assembly consisting of the *n* detection modules. These simulations assumed neutron incidence perpendicular on the converter plane and are performed by using the GEANT4 [49-52] software package. The main goal of these simulations was to find a reasonable balance between the number *n* of detection modules and the refined thickness of the $^{10}B_4C$ converter coating in the subsequent detection modules traversed by the neutron beam at the desired detection efficiency for a specific neutron spectrum foreseen for the MWPC-PSND.

The efficiency of the proposed design was investigated by building the theoretical model of the detector and tracking the slowing down of the ^{7}Li- and α-reaction products through the converter and counting gas until they came to total rest.

The energy deposited in the gas through ionization was used to generate the combined (both ions) pulse-height spectrum. The efficiencies represented graphically in Fig. 6 of the manuscript were calculated by taking the ratio between the total number of counts in the pulse-height spectra recorded for each configuration and the total number of incident neutrons impinging upon the detector. The results represent a measure for the absorption, conversion, and escape efficiency only, i.e., $\varepsilon_{abs} * \varepsilon_{conversion} * \varepsilon_{escape}$, not the total detection efficiency, ε_{det}, which also depends on the ability to collect the charge generated in the gas volume, $\varepsilon_{det} = \varepsilon_{abs} * \varepsilon_{conversion} * \varepsilon_{escape} * \varepsilon_{collection}$. Previous experience with operating a similar MWPC design indicated that the efficiency for collecting the charge generated in the gas is greater than 90 % [53]. Moreover, in the real detector, an energy threshold must be also applied to the individual pulses in order to eliminate those generated by the γ-background. Such a threshold was not considered in the present calculations. However, typical values for the n-γ discrimination threshold in the ^{10}B-based gas detectors lie between 100-150 keV, which leads to a reduction of the detection efficiency by less than 10%, as shown in Fig. 4 of [54].

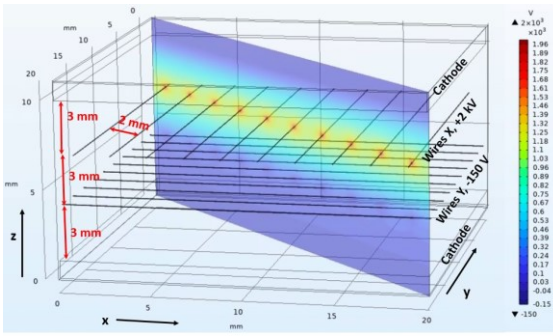

Fig. 5. COMSOL-simulations of the electric potential (V) (red=positive, blue=negative) for the detector design proposed in the present work. The detector design parameters are marked in the figure.

The electric field configuration for one x/y-wires-plane detector module under HV (U_x= +2000 V / U_y= -150 V) is presented in Fig.5. The electric field configuration inside one detection module had been calculated using the COMSOL-simulation-package and serves to visualise the E-field homogeneity and demonstrates the input configuration for the GEANT4 simulations.

Fig.6(A) represents the simulated efficiency contributions from each subsequent module consisting of a stack of 15. Each module contains two 1.2 µm-thick $^{10}B_4C$ converter layers. The calculations were performed with monochromatic neutrons at wavelengths 1, 2.5, 4 and 5 Å. The plots indicate that the efficiency contribution drops from one to the next module even though the modules contain a neutron absorbing coating of the same thickness. This behaviour can be observed for each of the four values of the neutron-energy considered in the calculations. The efficiency drop has its origin in the continuous extraction of neutrons from the transmitted neutron beam by every subsequent

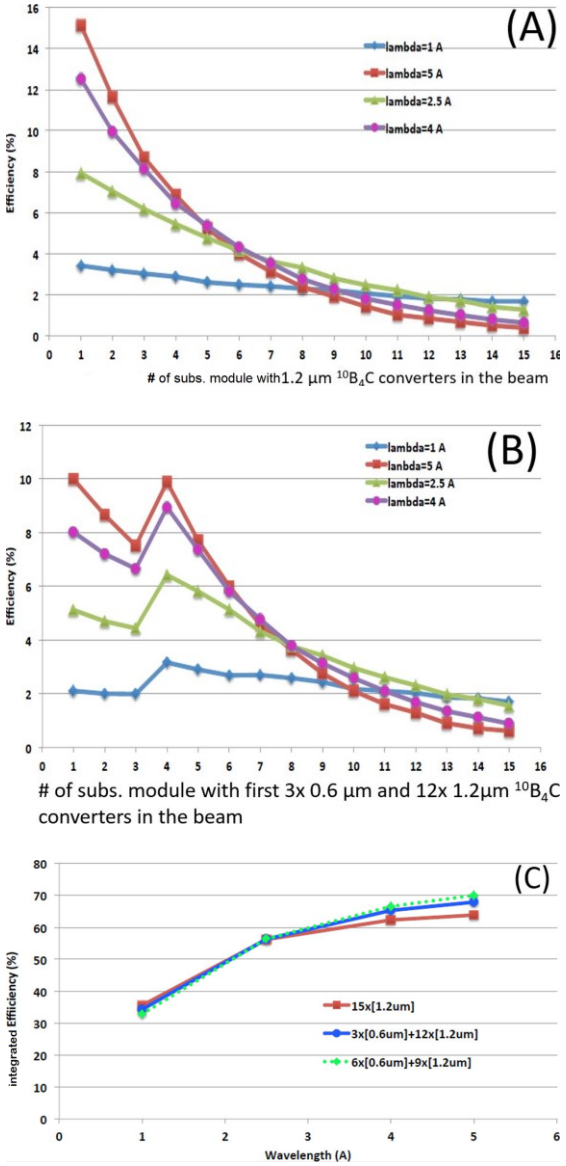

Fig. 6. (A) Efficiency contributions from single, subsequent detection modules consisting of two converters coated by 1.2 µm $^{10}B_4C$ for monochromatic neutrons at 1 Å (blue), 2.5 Å (green), 4 Å (violet) and 5 Å (red). The front $^{10}B_4C$-double layer is marked with the number "1". (B) Efficiency contributions of subsequent modules consisting of two different coating thicknesses of the $^{10}B_4C$ converters for monochromatic neutrons at 1 Å (blue), 2.5 Å (green), 4 Å (violet) and 5 Å (red). The first three modules have 0.6 µm and the further twelve modules have 1.2 µm thick $^{10}B_4C$-coatings. (C) Efficiency spectrum integrated over 15 modules with 1.2 µm thick $^{10}B_4C$ (red), over 3 modules coated by 0.6 µm and 12 modules coated by 1.2 µm thick $^{10}B_4C$ (red) and finally over 6 modules coated by 0.6 µm and 9 modules coated by 1.2 µm thick $^{10}B_4C$ (green; dashed).

module. This observation is in-line with the well-known Beer-Lambert-law for neutron absorption in matter. In Fig. 6(B) the individual efficiencies were simulated for the same neutron energies as in Fig. 6(A), but the thickness of the converter in the first three modules was reduced by a factor of two (i.e., 0.6 µm of $^{10}B_4C$) while

the thickness of all the other layers was left unchanged (1.2 µm of $^{10}B_4C$). Consequently, the efficiency contribution of the first three modules dropped down compared to Fig.6 (A). However, the 4th module and the following ones have a higher efficiency contribution when compared to the 4th module in Fig. 6(A): compare 10 % at 5 Å in Fig. 6(B) to 7 % at 5 Å in Fig. 6(A). Thus, the variation of the converter thickness leads to a change in the efficiency distribution over the entire detector stack, and consequently to a change in the count-rate per detection module. This effect can help improve both the local and global count-rate capability of the detector, as the number of detected neutrons is more evenly distributed over the first 4-5 modules and not anymore concentrated in the first two (see Fig. 6(B)). The spread of the count-rate over the depth of the detector becomes more important when operating at cold neutron energy. Cold neutrons have a high probability to be detected within a few µm of $^{10}B_4C$, leading to much larger count-rates in the first two detection modules compared to the subsequent ones. Furthermore, using thinner converter coatings in the detection modules that are first exposed to the neutron beam leads to a slight improvement of the overall detection efficiency (~8 %) for cold neutrons, as seen in Fig. 6(C).

In the thermal regime, however, a detector stack consisting of 15 detection modules, all comprising $^{10}B_4C$ converter layers with 1.2 µm thickness, has an overall detection efficiency that is slightly higher than the stacks built with converter $^{10}B_4C$-coatings of variable thickness. The explanation for this is that for higher energy neutrons, the ion-escape length dominates over the neutron-absorption length. For the low-energy neutrons, the conversion point is statistically closer to the converter surface and the ion-escape probability increases compared to the case of higher neutron energies. Numerical details of these considerations can be found in [2].

The results of these simulations indicate that the overall efficiency of the detector stack is influenced by reducing the thickness of the $^{10}B_4C$ converter coating applied on the first few modules located close to the entrance window of the detector. The economic advantage of doing this is that it reduces the sputtering (coating) time and the amount of converter material used in the coating process, with positive effects on the total costs and manufacturing time of the detector. However, this simulation case also makes it clear that the converter coating thickness in the stacked detection modules needs to be adapted to the neutron energy-range and application for which the detector is intended to be used. The simulated efficiency values are summarized in Tab.1.

Tab.1. Summary of plot Fig. 6(C).

Neut. wave-length [Å]	**15x [1.2 µm] $^{10}B_4C$ integr. efficiency [in %]**	**3x [0.6 µm] + 12x [1.2 µm] $^{10}B_4C$ integr. efficiency [in %]**	**6x [0.6 µm] + 9x [1.2 µm] $^{10}B_4C$ integr. efficiency [in %]**
1	36.6	34.8	32.8
2.5	56.8	56.9	56.9
4	62.5	65.7	66.5
5	63.6	67.7	69.9

2.3 Mechanical design and strain simulations of the detector modules and detector housing

The hardware exterior of the detector is a gas-tight housing. The detector housing represents the interface between the detector and the ambient space. It consists of three sub-components 1. neutron entrance window, 2. top-cover and 3. the back-plate. The functions of the first two components are a loss-free transmission of neutrons to the detection modules in the housing. The second function is the protection of the well-defined stopping-gas volume from changes of ambient conditions and parameters like temperature and atmospheric pressure. The back-plate has three functions. The first function is a mechanical, rigid support for the detection modules to ensure minimal displacement of wires and converters during transport and operation. The second function of the back-plate is to offer a mechanical interface and a distribution base for loads during vertical mounting of the detector in a support structure for operation at a beamline or for transportation purpose. Last but not least, the third function of the back-plate, is the provision of a mechanical platform for the electronic and media feedthroughs to the inside components like the wire-planes with their signal- and HV-lines and the detection modules with their gas- and USB-data-lines. The shape of these three mechanical sub-components, their material grade and thicknesses had been designed for ± 0.1 bar pressure difference between the ambient pressure (corresponding to the average air pressure in Lund/SWE of 1000 mbar) and the pressure of the stopping-gas inside the detector. The weight limitations for the whole detector assembly and the large surface area of the detector housing as well as high mechanical load resulting from the envisaged pressure difference of max. 0.1 bar between in- and outside of the detector, makes a (Computed Aided Design) CAD-supported design simulation essential. Therefore, the mechanical loads in the housing and particularly in the converter support-frames of the detection modules were simulated by means of the (Finite Element Method) FEM-techniques using the concept of the von-Mises-tension [55]. These simulations delivered the von-Mises tensions and the local deformations of the components at the operational conditions as presented in Tab.2

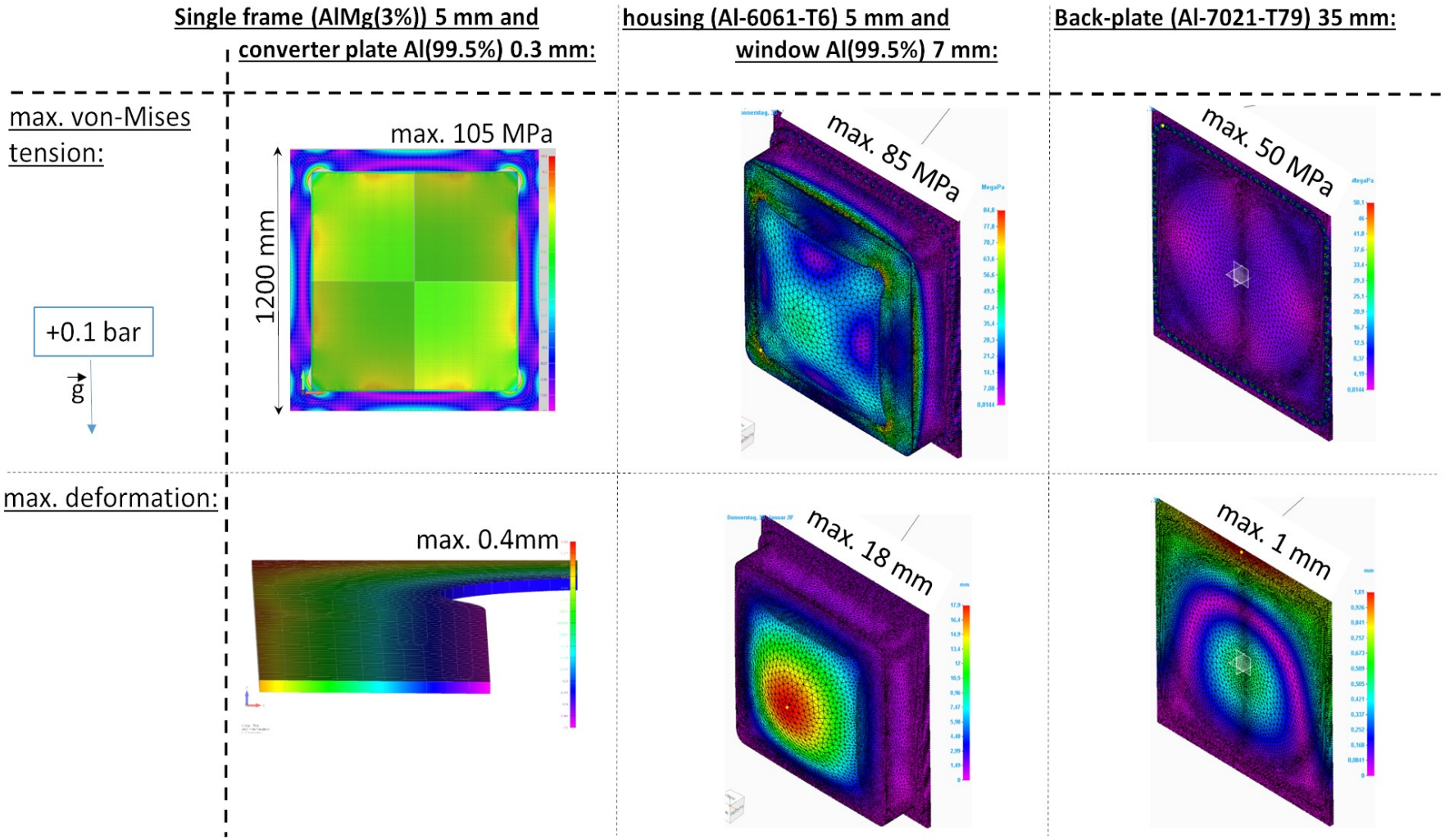

Tab. 2. FEM-simulations of the von-Mises-tension (top row) and deformation (bottom row) for: the single frame-converter element where the converter plate is clamped in the converter support frame (left column), the top housing with neutron entrance window (middle column) and back-plate (right column). The simulations were performed in gravity field and an overpressure of +0.1 bar in the detector housing as indicated on the left side in Tab.2.

for the corresponding envisaged material grades [56]. The FEM-simulations had been performed using the "Solid Edge ST(110.00.12.004 x64) FEMapp (11.3.1)"-software and the NX-Nastran (11.0) solver. For the operational parameters, it was assumed that the detector is erected vertically so that its entrance window surface normal is oriented orthogonally to the gravity (as indicated in Tab.2) and the ambient pressure is 0.1 bar higher than the stopping-gas pressure inside the detector. As described in reference [4], the 1m^2-large Al-converter plates coated by $^{10}B_4C$ were clamped on support frames, which ensure a flat mounting of the converter surface in front of the wire-planes inside the detection module. The result of the FEM-optimization processes for supporting the 0.3 mm thick converter (Al 99.5 %), is a 5 mm thick AlMg(3%) frame with a shape as presented in the column labelled "Single frame-converter plate" in Tab.2. The frame has inside rounded corners to redistribute and reduces the von-Mises-tensions to 105 MPa in this work piece. This shape should ideally offer the required stiffness for the envisaged converter flatness. The connected maximum deformation of the single frame and converter-plate assembly was calculated to about 0.4 mm at the outer edges of the converter and frame. This is expected to be in the acceptable range for operation.
For the top part of the housing, a 5 mm thick Al-6061-T6 base material and for the neutron entrance window a 7 mm thick Al(99.5%) plate turned out to be appropriate (see column "housing and window" in Tab.2). This choice of material thicknesses and grades lead to a maximal deformation in the centre of the window of 18 mm at an acceptable, von-Mises tension level of maximum 85 MPa. For the "Back-plate" the FEM-simulations yields a 35 mm thick Al-7021-T79 as a useful thickness and material grade (see column "Back-plate" in Tab.2). In this configuration, a deformation of 1 mm in the central region of the Back-plate at a maximal von-Mises tension of 50 MPa is expected. This tension is far below the considered material grade limits. These evaluations were performed for an overpressure of +0.1 bar in the housing compared to the outside pressure and in the gravity field oriented as above mentioned.

3 Conclusions

This parametric study demonstrate the technical feasibility of a 1m^2-size neutron detector for a perpendicular neutron incidence using stacked detection modules consisting of multi-wire detection planes confined between $^{10}B_4C$-coated converters. The conditions of operations (max. pressure difference and gravity field) had been considered in the design. The neutron-conversion and detection processes specific to the $^{10}B_4C$ converter coating and the characteristics of the Ar/CF_4-stopping-gas indicate that a converter-to-wire distance of 3 mm offers a sufficient high charge yield from both $^{10}B_4C$-converters on the detection wires of the x- and y-wire-plane in a single detection module. The ToF-timing precision of one detection module and therefore for the entire stacked detector assembly is consequently restricted to the neutron time-of-flight through the converter face-to-face distance of 9 mm. The position resolution of the detection wire-planes given by their 2 mm wire-pitch is not impaired by the pressure-range of the stopping-gas, which determine the maximal possible pressure load on the detector housing, as demonstrated in Sections 2.1 and 2.3. The thickness of the $^{10}B_4C$-converter in the stacked detection modules assembly was optimised for a specific use-case neutron spectrum with the help of GEANT4 simulations. The results of this calculation provides the refined values for the $^{10}B_4C$ coating thicknesses in the sequenced converters. The $^{10}B_4C$ thickness refinement leads to improved local and global count-rates loads at reduced manufacturing costs while still preserving the high overall detection efficiency of the entire detector assembly. Similar optimisations are also typically done for the gas-converter-based thermal neutron detectors such as ^{3}He-tubes, by carefully inspecting the dependence of the gas-pressure vs. neutron efficiency. As seen in Section 2.2, the integrated neutron efficiency that can be achieved with a detector assembly like the one described in the present work is similar to what is currently possible to achieve with the pressurized ^{3}He-detectors. The manufacturing of the required converter shapes and sizes as well as the wire-planes is feasible by using conventional production techniques. The required stabilities of involved materials for the operational case of the detector are not in conflict with the commercially available lightweight material grades as shown in chapter 2.3. Hereon, formerly HZG and GKSS, successfully applied the MWPC-technology with 2D-delay-line read-out to position-sensitive Neutron detectors based on ^{3}He in the past to the REFSANS and SANS-1 instruments at MLZ [57] as well as at the ARES instrument of the Geesthacht Neutron Facility (GeNF) at FRG-1 [58]. These results motivated the researches to make the next certainly challenging but interesting step and to combine the delay-line technology with the solid state $^{10}B_4C$-conveters. A successful realization of these kind of detectors would merge a 2D-sensive MWPC-neutron detector with a relative small number of read-out channels and with an affordable ^{3}He-free neutron converter technology. This detector design would then contribute to overcome the "^{3}He-crisis" mentioned in Chapter 1.1. The applications of these kind of detector technology is aiming for diffraction instruments with moderate position resolution requirements (≥ 2mm) at ESS and of cause at other neutron research facilities.

The acknowledgements of the authors goes to the ESS ERIC for their ESS in-kind program offering the technically challenging research topic as well as to the German Federal Ministry of Education and Research (BMBF) for the financial support.

References

1. G. Nowak et al., J. Appl. Phys. **117**, 034901 (2015)
2. F. Piscitelli, et al., J. Instr. **13**, P05009 (2018)

3. European Patent Application 2 997 174 (14.07.2014)
4. European Patent Application 3 662 306 (10.03.2021)
5. G. Charpak, et al., Nucl. Instrum. Meth. **62**, 262 (1968)
6. F. Sauli, "Principles of Operation of Multiwire Proportional and Drift Chambers", Lecutres given in the Academic Training Programme of CERN, Geneva (1977)
7. https://www.ill.eu/de/neutrons-for-society/neutron-technology/detectors
8. Su-Ann Chong et al., Nucl. Instrum. Meth. A, **1039**, 167052 (2022)
9. J.-F. Moulin et al., Journal of Large-Scale Research Facilities, **1**, A9 (2015)
10. K. Toh et. al., Journal of Physics: Conference Series, **528**, 012045 (2014)
11. K.H. Andersen et al., Nucl. Instrum. Meth. A, **957**, 163402 (2020)
12. M. O. Klein, Ph.D.-Thesis, Ruprecht Karls Universität, Heidelberg, (2000)
13. G. Mauri et al., EPJ Techniques and Instrumentation, **6**:3 (2019)
14. R. Arnaldi, et al., Nucl. Instrum. Methods Phys. Res., Sect. B **213**, 284–288 (2004)
15. J. H. Coon, Phys. Rev. **75**, 1355 (1949)
16. J. A. Bistline Jr., The Rev. Sci. Instr. **19**, 12 (1948)
17. G. F. Knoll, "Radiation Detection and Measurement", 4th ed. John Wiley & Sons, p. 534 (2010)
18. D. A. Shea and D. Morgan, Report No. R41419, (2010)
19. See http://eval.esss.lu.se/cgi-bin/public/DocDB/ShowDocument?docid=274, "European Spallation Source—Technical Design Report", ESS-2013-001 (2013)
20. C. Höglund et al., J. Appl. Phys. **111**, 104908 (2012)
21. C.-C. Lai et al, Surf. Coat. Tech. **433**, 128160 (2022)
22. M. Anastasopoulos et al., J. Inst. **12**, P04030 (2017)
23. J. C. Lacy et al., IEEE Nucl. Sci. Conf. Rec., 3971 (2010)
24. J. C. Lacy et al., IEEE NSS MIC Conference Seattle, WA, USA, (2014)
25. H. J. Taylor, Proc. Phys. Soc. **47**, 873 (1935)
26. B.T.M. Willis and C. J. Carlile, „Experimental Neutron Scattering", Oxford University Press (2009)
27. I. Stefanescu et al., J. Inst. **12**, P01019 (2017)
28. J. Fenske et al., Journal of Physics: Conference Series, **746**, 012009 (2016)
29. Moriai, S. Torii, H. Suzuki, S. Harjo, Y. Morii, M. Arai, Y. Tomota, T. Suzuki, Y. Akiniwa, H. Kimura, K. Akita: Physica B, **385-386**, 1043-1045 (2006)
30. W. Kockelmann, S.Y. Zhang, J.F. Kelleher, J.B. Nightingale, G. Burca, J.A. James, Physics Procedia, **43**, 100-110 (2013)
31. M.A.M. Bourke, D.C. Dunand, and E. Ustundag, Appl. Phys. A: Mat. Sci. Proc. **74**, 1707-1709 (2002)
32. J. R. Santisteban, M. R. Daymond, J. A. James and L. Edwards, J. Appl. Cryst., **39**, 812-825 (2006)
33. X.-L. Wang, T.M. Holden, G.Q. Rennich, A.D. Stoica, P.K. Liaw, H. Choo, C.R. Hubbard, Phys. B: Cond. Mat., **385-386**, 673-675, (2006)
34. M. T. Hutchings, P. J. Withers, T. M. Holden and T. Lorentzen, "Introduction to the characterization of residual stress by Neutron diffraction", Taylor & Francis Group, LLC, (2005)
35. J. Lindsay et al., CERN 74-12 (1974)
36. A. Epstein and C. Boulin, IEEE Trans. Nucl. Sci. **43**, 159 (1996)
37. J. B. Khazaie and C. Boulin, IEEE Trans. Nucl. Sci. **43**, 197 (1996)
38. J. B. Khazaie and C. Boulin, IEEE Trans. Nucl. Sci. **43**, 193 (1996)
39. G. Pahl und W. Beitz, „Konstruktionslehre" - Grundlagen, 7. Auflage. Springer Verlag, (2007)
40. R. G. Budymas and J. K. Nisbett, "Shigley's Mechanical Engineering Design", TBS; 8th edition (2006)
41. W. H. Bragg, Phil. Mag. **10**, (57): 318 (1905)
42. J. P. Biersack and L. Haggmark, Nucl. Instrum. Meth. **174**, 257 (1980)
43. J. F. Ziegler, J. P. Biersack, and U. Littmark, "The Stopping and Range of Ions in Solids", Pergamon, New York, Vol. 1. (1985)
44. F. Piscitelli et al., J. Inst. **8**, P04020 (2013)
45. J. F. Ziegler, M. D. Ziegler and J. P. Biersack, Nucl. Instrum. Meth. Phys. Res. Sect. B, **268**, 1818 (2010)
46. http://www.srim.org/;
47. TRIM/SRIM, Textbook on http://www.srim.org/
48. Stefanescu et al., J. Inst. **14**, P10020 (2019)
49. https://geant4.web.cern.ch/node/1
50. S. Agostinelli et al., Nucl. Instrum. Meth. A, 506, **3**, 250–303 (2003)
51. J. Allison et al., IEEE Trans. Nucl. Sci. 53, **1**, 270-278 (2006)
52. J. Allison et al., Nucl. Instrum. Meth. A, **835**, 186-225 (2016)
53. J. Orban et al., Nucl. Instrum. Meth. A, **632**, 124 (2011)
54. I. Stefanescu et al., J. Inst. **8**, P12003 (2013)

55. R. v. Mises, Z. Angew. Math. Mech. **8**, 161 (1928)
56. F. U. Mathiak,“ Die Methode der finiten Elemente (FEM)“, Neubrandenburg (2010)
57. R. Kampmann, M. Marmotti, M. Haese-Seiller, V. Kudryashov, Nucl. Instrum. Meth. A, **529**, 342-347 (2004)
58. M. Marmotti, M. Haese-Seiller, R. Kampmann, Physica B, **276-278**, 210-211 (2000)